LCC- 0061
May 2001

Linear Collider Collaboration Tech Notes

Lattice Description for NLC Damping Rings at 120 Hz

Andrzej Wolski

Lawrence Berkeley National Laboratory

Abstract: We present a lattice design for the NLC Main Damping Rings at 120 Hz repetition rate. A total wiggler length of a little over 46 m is needed to achieve the damping time required for extracted, normalized, vertical emittance below 0.02 mm mrad. The dynamic aperture (using a linear model for the wiggler) is in excess of 15 times the injected beam size. The principal lattice parameters and characteristics are presented in this note; we also outline results of studies of alignment and field quality tolerances.

Lattice Description for NLC Main Damping Rings at 120 Hz

Andrzej Wolski
Lawrence Berkeley National Laboratory

April 27th, 2001

Abstract

We present a lattice design for the NLC Main Damping Rings at 120 Hz repetition rate. A total wiggler length of a little over 46 m is needed to achieve the damping time required for extracted normalized vertical emittance below 0.02 mm mrad. The dynamic aperture (using a linear model for the wiggler) is in excess of 15 times the injected beam size. The principal lattice parameters and characteristics are presented in this note; we also outline the results of studies of alignment and field quality tolerances.

1 Introduction

The main requirement for the NLC Main Damping Rings is to accept an injected beam from the source with large transverse emittances, and reduce the emittances for injection into the main linacs. Losses during the injection, damping and extraction processes must be kept to a minimum, both to avoid radiation loads within the damping ring, and to deliver the maximum number of particles to the interaction point; losses will be determined by the quality of the injection and extraction systems, and the physical and dynamic apertures within the ring. Design principles for linear collider damping rings have been discussed elsewhere[1]. The design is constrained by the injected and extracted emittances, the pulse length, and the repetition rate. A significant amount of design work has already been carried out for the NLC Main Damping Rings at 120 Hz repetition rate, which have shown solutions for the damping rate[2] and the dynamic aperture[3] separately; our latest design meets both design criteria.

2 Lattice Parameters

The "external" parameters driving the lattice design are shown in Table 1. The principal lattice parameters are shown in Table 2.

Table 1: "External" parameters.

Bunches per train	N_b	190
bunch-to-bunch spacing[a]	τ_b /ns	1.4
kicker rise/fall time	τ_k /ns	65
collider repetition rate	f /Hz	120
injected horizontal/vertical emittance	$\gamma\varepsilon_{inj}$ /mm mrad	150
extracted horizontal emittance	$\gamma\varepsilon_{x,ext}$ /mm mrad	<3
extracted vertical emittance[b]	$\gamma\varepsilon_{y,ext}$ /mm mrad	<0.02

Table 2: Principal lattice parameters.

Energy	E /GeV	1.98
Number of bunch trains stored	N_{train}	3
Vertical store time [a]	N_τ	4.97
Circumference	C /m	299.792
Arc cell type		TME
Arc cell length	/m	5.120
Length of each straight	/m	62.856
Number of arc cells		34 + 4×½
Main arc dipole gradient	k_1 /m^{-2}	-1.0
Horizontal tune	Q_x	27.2616
Vertical tune	Q_y	11.1357
Natural horizontal chromaticity	ξ_x	-37.12
Natural vertical chromaticity	ξ_y	-28.24
Normalized natural emittance	$\gamma\varepsilon_0$ /mm mrad	2.17
Damping times	$\tau_x, \tau_y, \tau_\varepsilon$ /ms	4.85, 5.09, 2.61
Assumed coupling	κ	0.5 %
Extracted horizontal emittance	$\gamma\varepsilon_{x,ext}$ /mm mrad	2.18
Extracted vertical emittance	$\gamma\varepsilon_{y,ext}$ /mm mrad	0.019
Ratio of vertical equilibrium to extracted emittance	$\varepsilon_{y0}/\varepsilon_{y,ext}$	0.72
Momentum compaction	α	2.95×10^{-4}
RF voltage	V_{rf} /MV	1.07
RF acceptance	ε_{rf}	1.5 %
Rms energy spread	σ_δ	0.0909 %
Bunch length	σ_z /mm	3.60
Synchrotron tune	Q_s	0.003496
Wiggler peak field	$\hat{B}_w$ /T	2.15
Wiggler period	λ_w /m	0.27
Wiggler total length	L_w /m	46.238
Integrated wiggler field	$\int \hat{B}_w^2 ds$ /T^{2}m	106.866
Energy loss/turn from dipoles	U_0/keV	247
Energy loss/turn from wiggler	U_w/keV	530
Total energy loss/turn	$U_0 + U_w$ /keV	777
Energy loss ratio	F_w	2.15
Dynamic aperture	A	$>15\sigma_{inj}$

[a] The vertical store time is the number of vertical damping times for which each train is stored.

Lattice functions for different sections of the lattice are shown in Figure 1 through Figure 4 below. Note that the main arc dipoles have a horizontally defocusing gradient, with a normalized value $k_1 = -1.0\ \mathrm{m}^{-2}$.

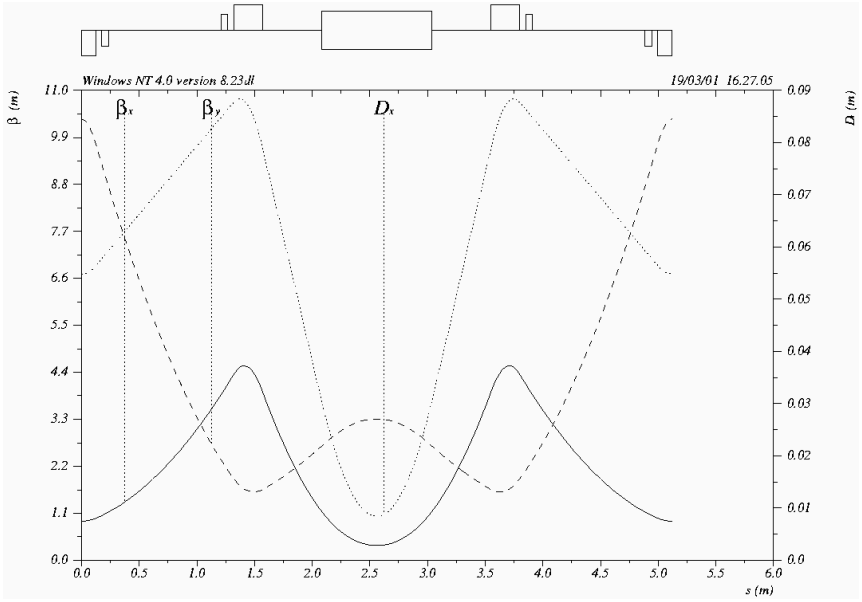

Figure 1

Lattice functions in an arc (TME) cell.

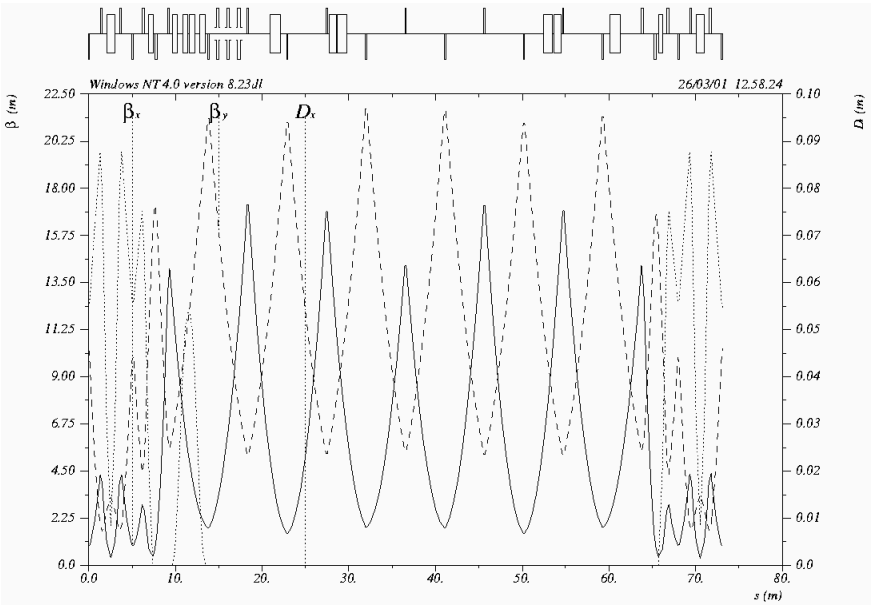

Figure 2

Lattice functions in the injection/extraction straight. A full TME cell is shown on either end of the straight. The circumference correction chicane appears as a sequence of four dipoles towards the left side of the diagram. Other components shown are (in sequence) the RF cavities, the extraction kicker, the extraction septa, the injection septa, the injection kicker.

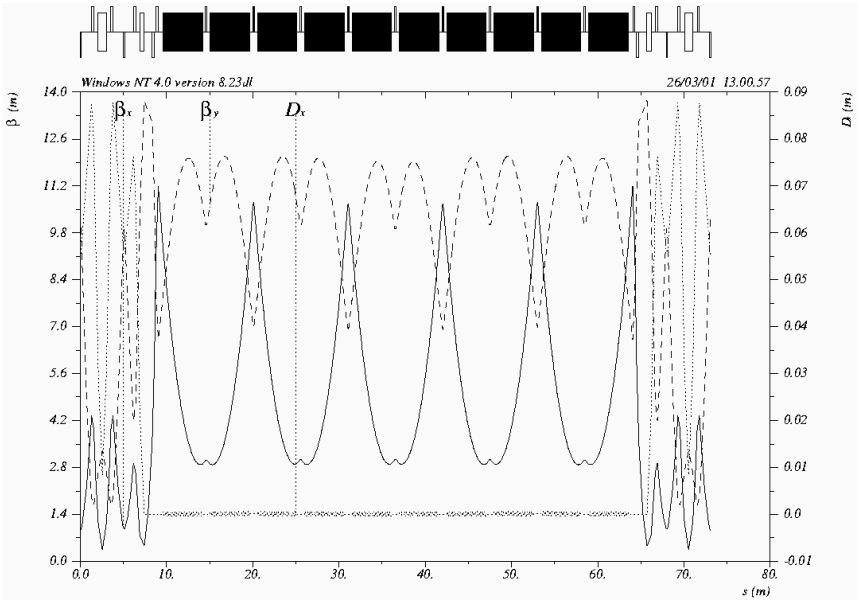

Figure 3

Lattice functions through the wiggler straight. A full TME cell is shown on either end.

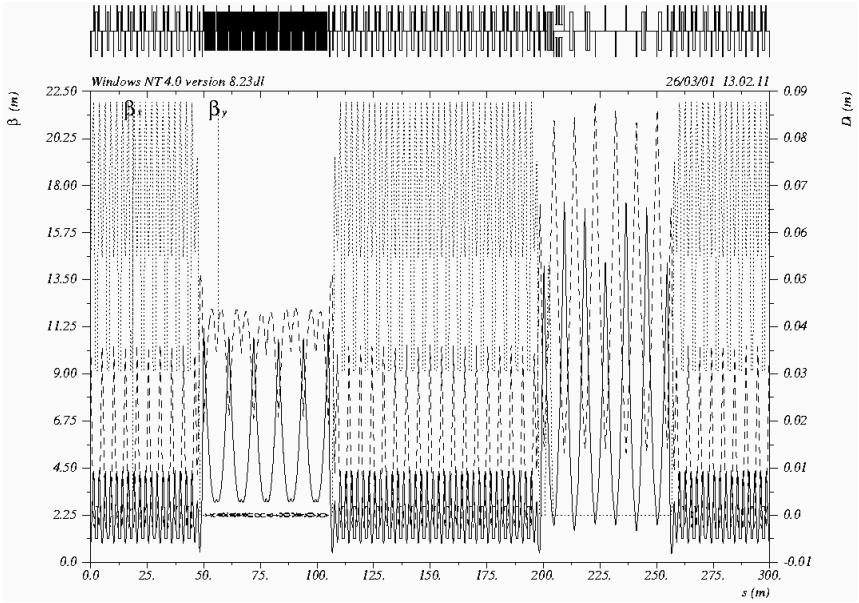

Figure 4

Lattice functions for the complete lattice.

Note that the total circumference is slightly larger than the 296.43 m minimum required to accommodate three bunch trains (190 bunches at 1.4 ns separation) with 65 ns kicker rise/fall time; the additional circumference was required to meet the constraints on beta functions and phase advances in the straight sections. However, the difference between the actual and minimum circumference is of the order 1%, and does not have a significant effect on the damping times or the extracted emittance. The actual circumference gives a harmonic number of 714, where the RF frequency is 714 MHz, so the revolution period is exactly 1 μs.

3 Chromatic Properties

The sextupoles are adjusted to give zero first-order chromaticity, although there remains a residual tune shift with momentum, as a result of higher order chromaticity. The variation of horizontal and vertical tune with momentum deviations up to ±1.5% are shown in Figure 5, and the working point in tune space is shown in Figure 6.

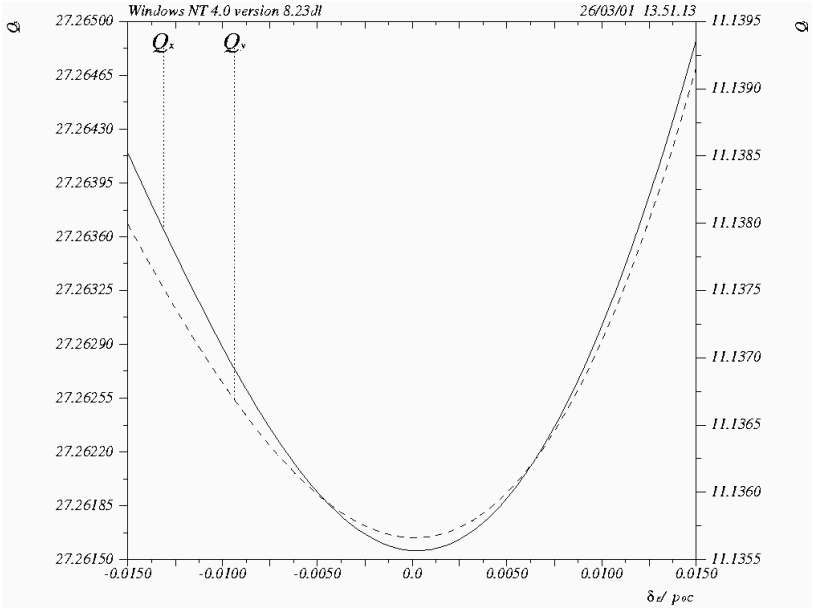

Figure 5

Variation of tunes with momentum, up to ±1.5% momentum deviation.

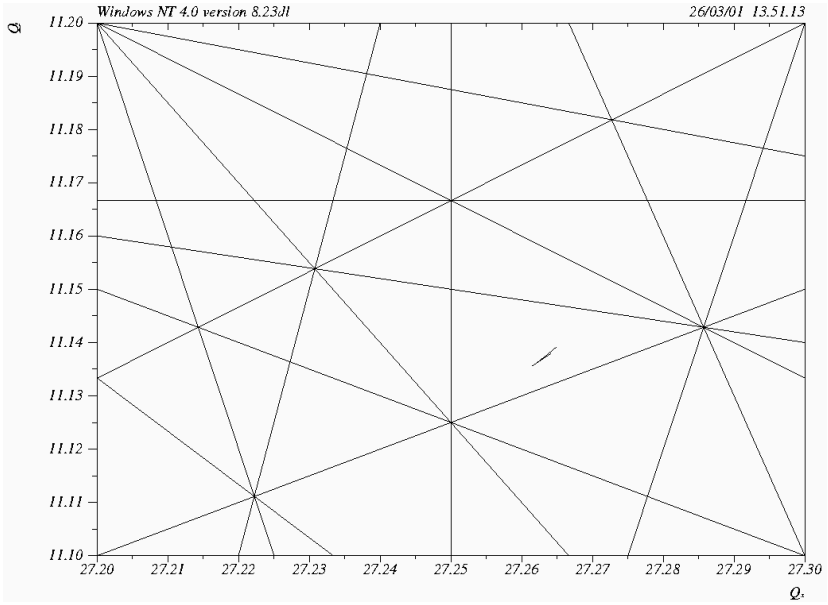

Figure 6

Working point of the lattice in tune space. The working point line shows variation of the tune with momentum deviations up to ±1.5%. Resonance lines up to sixth order are shown.

The lattice tunes have a strong effect on the magnet alignment tolerances, and integer and half-integer values in particular are to be avoided. In this respect, the present working point appears reasonable. The nearest coupling resonance is the third order difference resonance $2Q_y - Q_x$. We have found that the best tune from point of view of dynamic aperture is placed directly on this resonance, but this is incompatible with the requirement for very low coupling. The working point we have selected, we hope will give a reasonable compromise between dynamic aperture and coupling.

4 Dynamic Aperture

4.1 Dynamic Aperture of the Bare Lattice

The damping ring must have a good dynamic aperture to minimize particle loss, particularly during injection. The aperture is limited by nonlinear lattice elements, in particular the sextupoles, which are used in the dispersive regions (the arcs) to correct chromaticity, and tuned to give the lattice zero chromaticity. The nominally linear elements, such as the dipoles, quadrupoles and wiggler, may also have nonlinear components as a result of systematic and random field errors; these will also affect the dynamic aperture, and the allowable reduction in the aperture is a consideration for setting the tolerances on the field quality in these elements. For the present, however, we consider only nonlinear effects arising from the sextupoles.

If the straight sections are assumed to contain only linear elements, and are tuned to give phase advances close to an integer horizontally and vertically, then the dynamics of the lattice reduces to the dynamics of the TME cell. This has been achieved in the current lattice design, with the phase advances over both straights close to 3.0 horizontally and 1.0 vertically. Unfortunately, the integer phase advance gives large chromaticity (-4.92 and -5.25 horizontally and vertically in the wiggler straight, and -6.17 and -4.12 in the injection/extraction straight), so there is significant variation from the integer condition for modest momentum deviations. This effect is expected to limit the momentum acceptance of the lattice.

Studies of the nonlinear effects of the wiggler field are in progress[4]. The wiggler is expected to limit the dynamic aperture, both through direct effects of its nonlinear field, and also in the disruption of the integer phase advance across this straight; this technique to restore the periodicity of the lattice is only truly effective when there are no nonlinear elements in the relevant section. We have attempted to reduce the peak beta functions in the wiggler to values as low as possible, consistent with constraints indicated above. Currently, the vertical beta functions take a maximum value of 12 m, which gives an injected beam size of 0.68 mm. The physical aperture in the wiggler is 8.0 mm, or 11.8 times the injected beam size; thus the aperture limiting the transverse acceptance is physical rather than dynamic. Results of tracking studies presented here do not include the effects of physical collimation. To reduce the radiation load on the wiggler, it may be necessary to collimate the beam before injection into the damping ring; further studies will be carried out to evaluate the need for collimation.

Horizontal phase space portraits are shown in Figure 7, and vertical phase space portraits in Figure 8, for a single arc cell and for the full lattice. The portraits for a single cell are

similar to those for the full lattice, since the straight sections are tuned to integer phase advances.

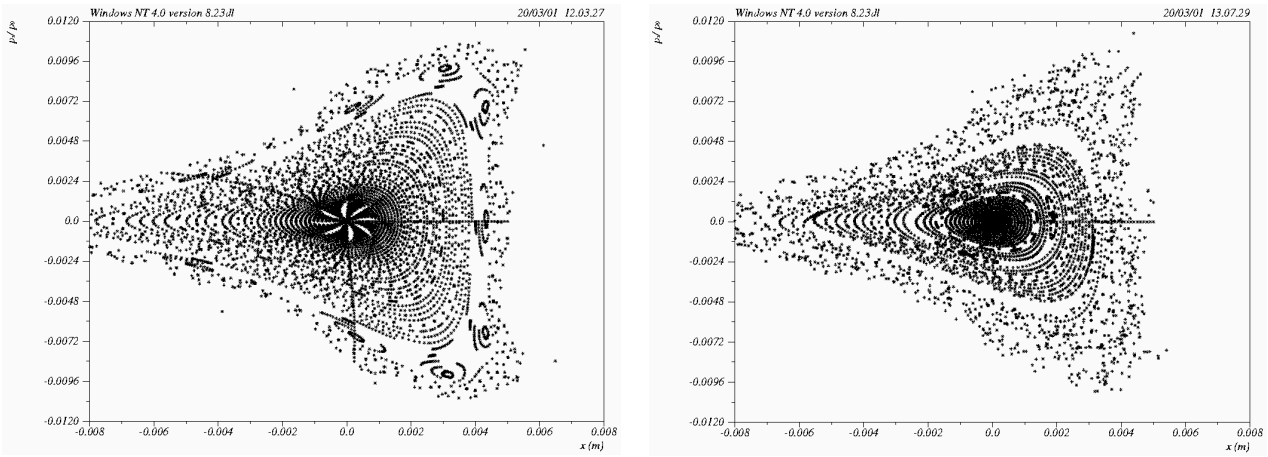

(a) (b)

Figure 7

Horizontal phase space portraits for (a) a single arc cell and (b) the full lattice. The observation point is the center of the DQUAD in an arc cell (as shown in Figure 1), where β_x = 0.991 m.

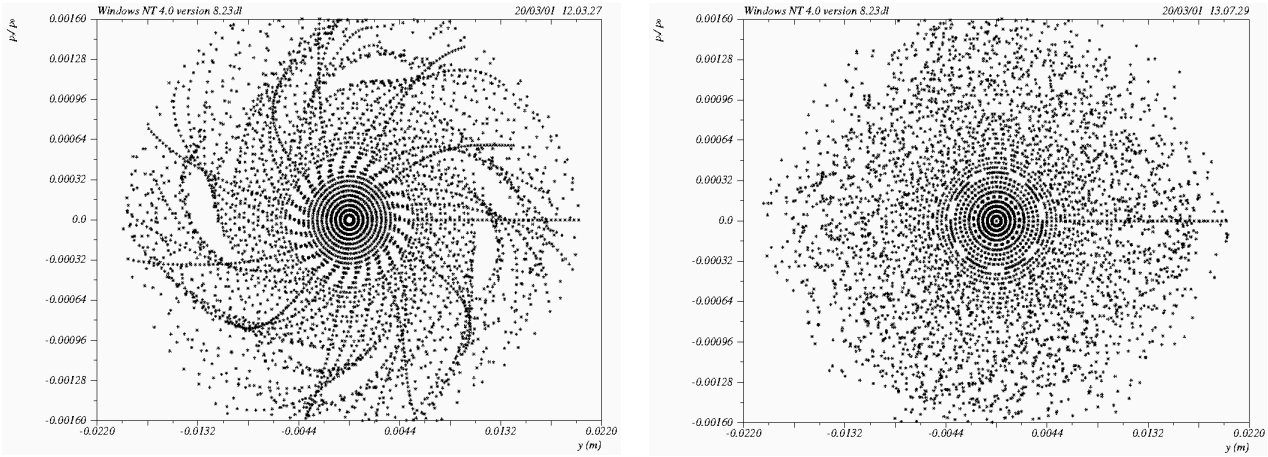

(a) (b)

Figure 8

Vertical phase space portraits for (a) a single arc cell and (b) the full lattice. The observation point is the center of the DQUAD in an arc cell (as shown in Figure 1), where β_y = 10.391 m.

Optimization of the dynamic aperture has been carried out pragmatically on a single TME cell, by adjusting the working point, and the phase advance between the sextupoles, to identify a region that gives good horizontal and vertical stability. However, a rigorous scan of tune space has not been carried out. Previous lattice designs have shown significant benefit in stabilizing the dynamics, from the gradient in the main bending magnets, and we have maintained the value k_2 = -1.0 m^{-2} used in the 180 Hz design[5], for example.

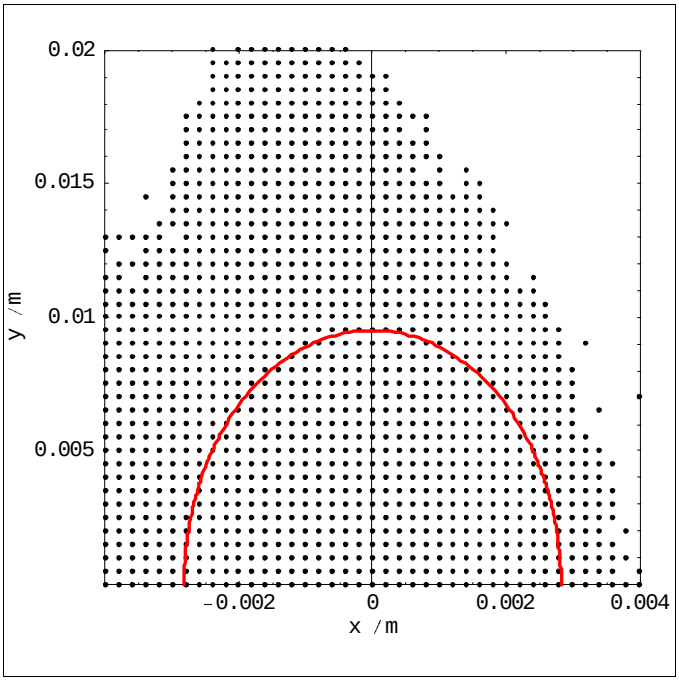

Figure 9

Dynamic aperture of the full lattice, with the wiggler modeled as a linear element. The particles were tracked through 500 turns, with the observation point at the center of the DQUAD in an arc cell, where β_x = 0.911 m and β_y = 10.391 m. The half ellipse shows 15 times the injected beam size.

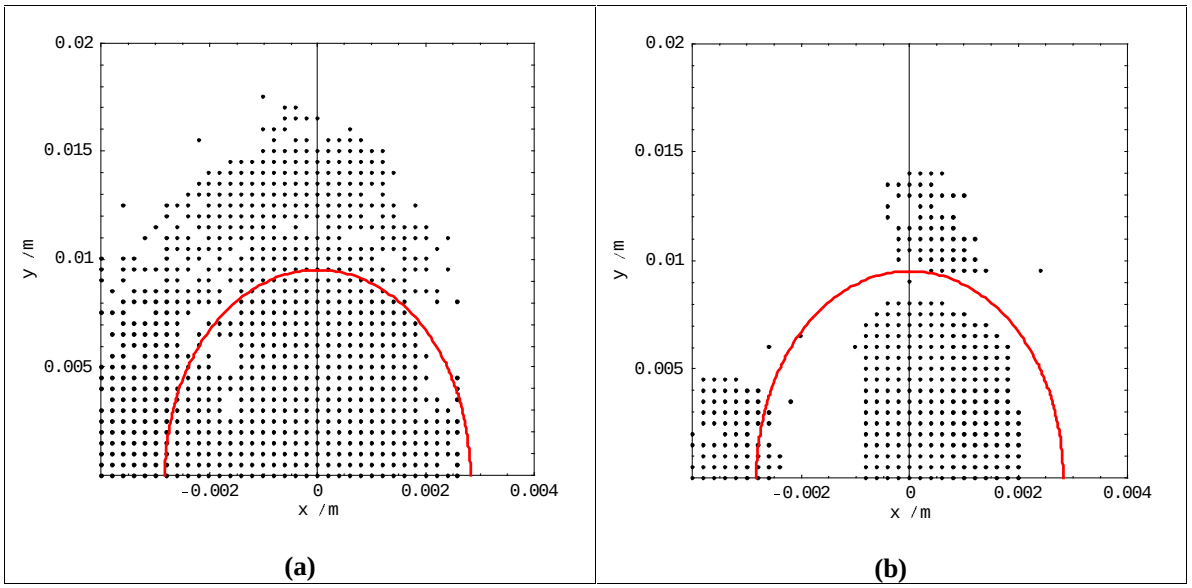

Figure 10

Dynamic aperture of the full lattice for momentum deviations (a) +0.5% and (b) +1.0%, using the same conditions as Figure 9.

A dynamic aperture plot for the full lattice is shown in Figure 9. Again, we emphasize that the plot has been produced by tracking the wiggler as a linear element. Figure 10 shows the dynamic aperture for particles with +0.5% and +1.0% momentum deviation (plots for negative momentum deviation are similar); as expected, we see that the lattice has a limited dynamic momentum acceptance, although it is not clear at present whether this will restrict the performance of the ring in terms of the injection efficiency. To investigate this, we propose further studies, involving tracking of realistic particle distributions through the lattice.

4.2 Dynamics in the Arc Cells

The dynamic aperture is limited by the nonlinearities in the arc cells, and the matching across the straight sections. Our present strategy is to make the straight sections "invisible" by tuning the phase advances to integer multiples of 2π, so we must look at the arc cells if we are to improve the dynamic aperture significantly. At present, we simply characterize the arc cells in terms of the tune dependence on amplitude.

The tune shifts with amplitude in the horizontal and vertical planes are shown in Figure 11 and Figure 12 respectively. A quartic fit is made to the data points, and in both cases, the tune shifts with amplitude are moderate, and comparable to the values seen in the 180 Hz lattice, where a good dynamic aperture was also achieved.

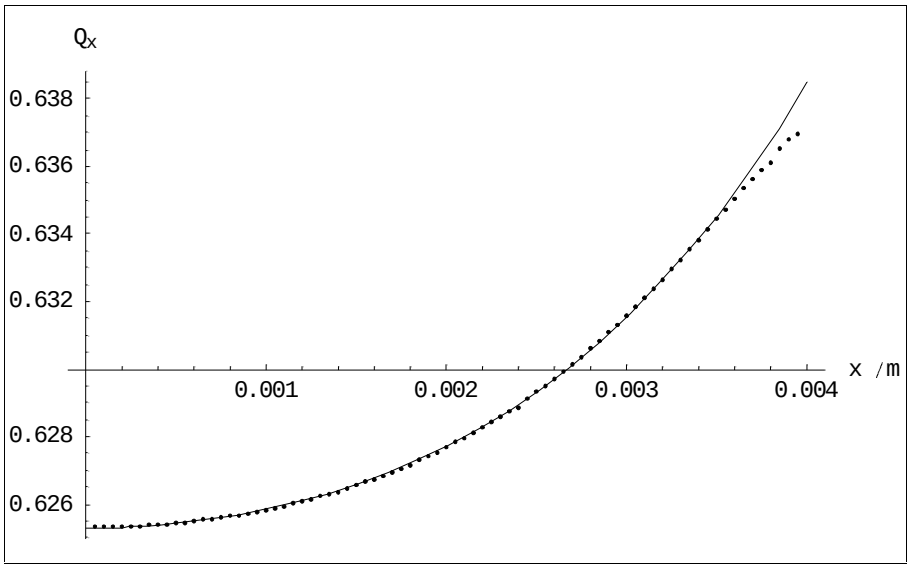

Figure 11

Horizontal tune shift with amplitude. The data points are fitted with a quartic curve, of the form $0.6253 + 526.3\,x^2 + 1.862\times10^7\,x^4$.

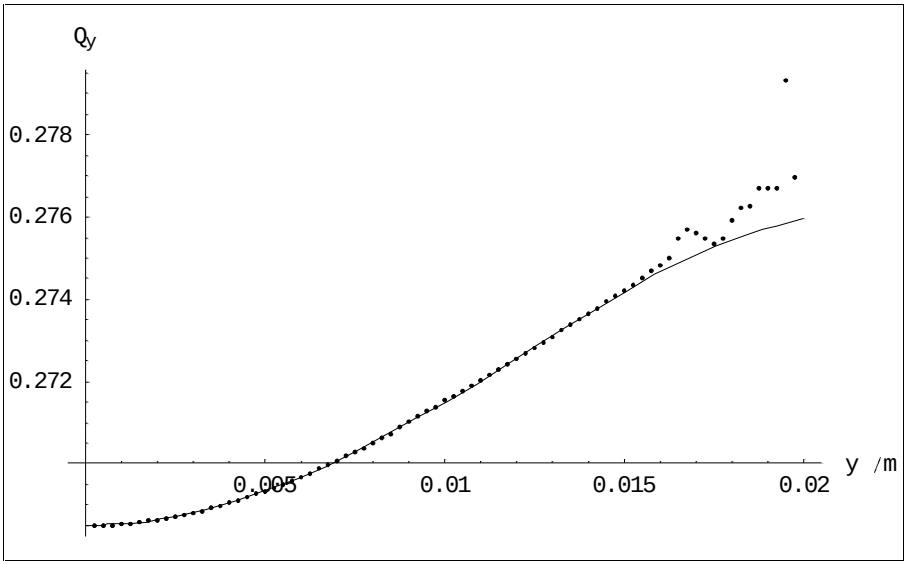

Figure 12

Vertical tune shift with amplitude. The data points are fitted with a quartic curve, of the form $0.2685 + 33.68\, y^2 - 3.771\times10^4\, y^4$.

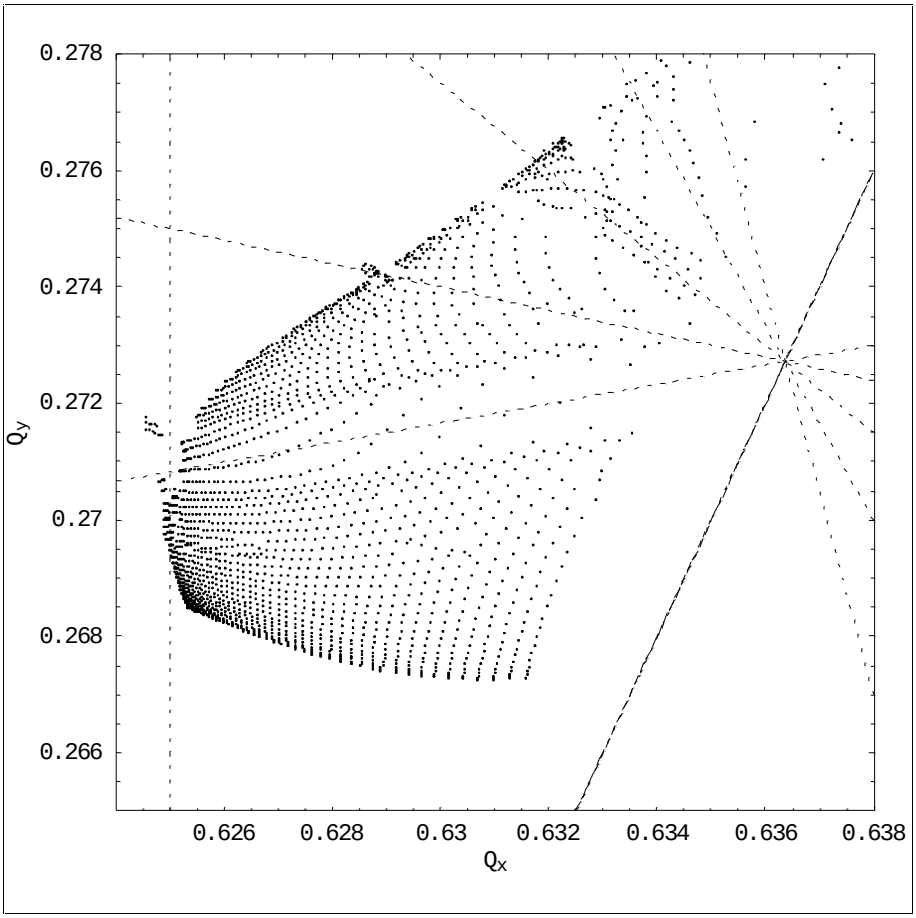

Figure 13

Frequency map analysis of an arc cell. Resonance lines up to eighth order are shown.

More information on the dynamics can be revealed by a frequency map analysis; this is shown in Figure 13. The plot is produced by setting up a regular grid of 4000 particles in co-ordinate space, from –2 mm to +2 mm horizontally, and from 0 mm to 3 mm vertically. The particles are tracked for 256 passes through an arc cell, and the tunes determined by Fourier analysis. Resonance lines up to eighth order are shown on the plot. Strongly driven resonances appear as disruptions to the regular array of points in frequency space; it appears that the current working point is some distance from the nearest driven resonance lines.

4.3 Effects of Systematic Field Errors

Nonlinear fields in the dipoles and multipoles will lead to a reduction in the dynamic aperture; we can set tolerances on the multipole components in the main magnets, based on the assumption that a reduction of the dynamic aperture below fifteen times the injected beam size will lead to a significant degradation of the damping ring injection efficiency. Higher order multipole field components can arise either systematically from design limitations (for example, from the finite extent of the pole pieces), or randomly from construction errors. Tolerances for the systematic errors are important at the design stage, so we consider these first. Our purpose is not to attempt a complete analysis of the dynamical effects of systematic field errors, but to perform an initial investigation, in order to set parameters for magnet design. As information becomes available on the magnitudes of different components likely to be present in each different type of magnet, a more thorough study can be undertaken.

4.3.1 Systematic Field Errors in the Main Arc Dipoles

Field errors in the main arc dipoles are most easily specified as absolute variations from the ideal field, where the ideal field includes both the 1.2 T main field and the gradient of $-6.605\ \mathrm{Tm}^{-1}$. The variation is necessarily a function of position; in practice, we find that the exact form of the variation is less important than the scale, i.e. the combined effects of the multipole components are important, whereas the way in which the effects are apportioned between components is less so. For simplicity, at this stage we assume that straightforward focusing errors arising from quadrupole field variations may be corrected by adjusting the tune and lattice functions. Thus, we consider the error effects arising from sextupole and higher order components.

Figure 14 shows the variation in field strength (expressed as a percentage of the main field at that point) that might arise from sextupole, octupole and decapole components. The harmonic fraction gives the field strength arising from each component as a fraction of the main field. We have investigated a variety of field strengths, distributed between components in a number of different ways, and find that a field variation of less than 6×10^{-4} T at 0.016 m (the internal beam pipe radius) is required to ensure a dynamic aperture in excess of fifteen times the injected beam size. We emphasize that the absolute field variation appears to be the significant quantity affecting the dynamic aperture, rather than the relative contributions of different components.

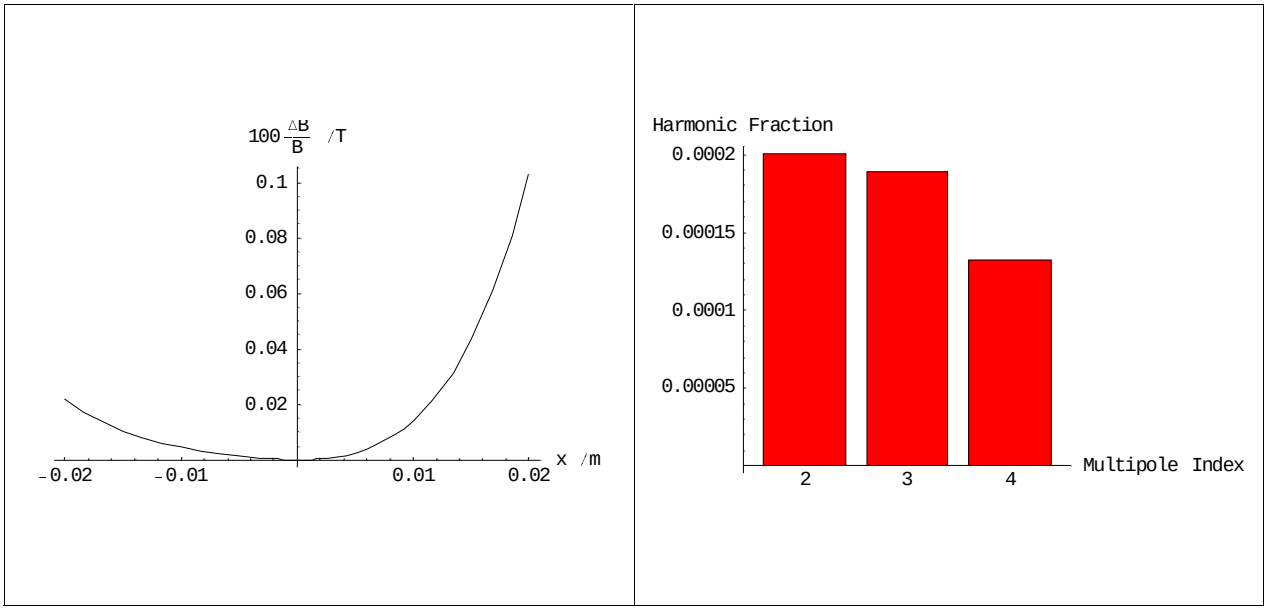

(a) (b)

Figure 14

(a) Variation in field strength in main arc dipoles, arising from (b) sextupole, octupole and decapole components. The harmonic fraction gives the field strength of each component as a fraction of the ideal field, at a radius of 0.016 m.

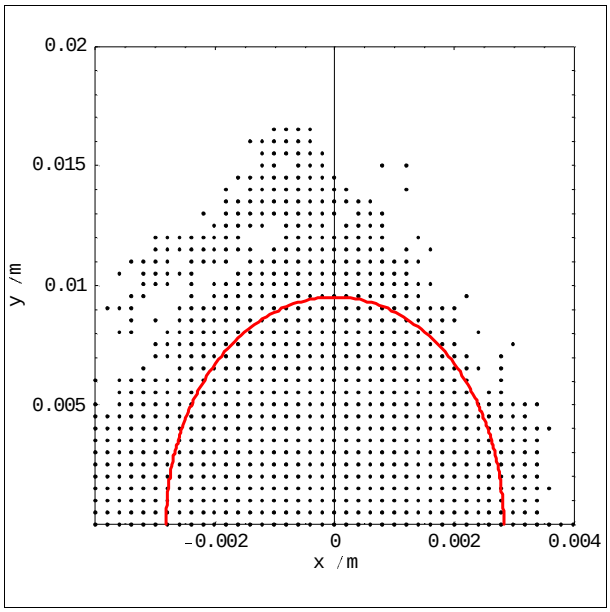

Figure 15

Dynamic aperture with systematic errors shown in Figure 14 applied to the main arc dipoles.

4.3.2 Systematic Field Errors in the Quadrupoles

The significant parameter for dynamics in a quadrupole is the field gradient; we therefore consider the effects of higher order components in terms of variations in the gradient, rather than variations in the absolute field strength. We assume that all the quadrupoles

will be ideal, in the sense that symmetry of the poles will restrict the allowed multipole components to n = 5, 9, 13… (where n = 1 for a quadrupole, and n = 2 for a sextupole). We again find that the total variation in the gradient is important, rather than the relative contributions of different components. The variation arising from a single n = 5 component, with $k_5 = 1.5\times10^5$ m^{-4} k_1, is shown in Figure 16 (a). We note that the total variation in the gradient at radius r_0 is given by:

$$\frac{\Delta g}{g} = \frac{1}{k_1}\sum_n \frac{k_n r_0^{n-1}}{(n-1)!}$$

Thus, at the internal beam pipe radius of 0.016 m, the variation in the quadrupole gradient is 0.04%, and at the pole tip (0.020 m), the variation is 0.1%.

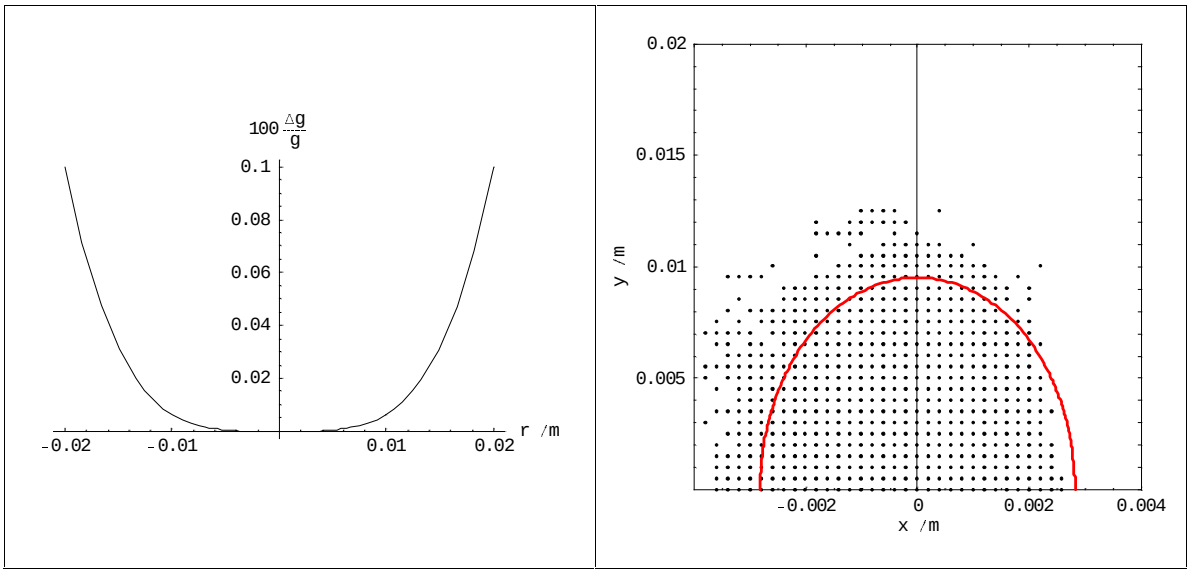

(a) (b)

Figure 16

(a) Variation in quadrupole gradient arising from a single multipole component $k_5 = 1.5\times10^5$ m^{-4} k_1, and (b) resulting dynamic aperture

The dynamic aperture for the lattice with systematic gradient error in the quadrupoles only, is shown in Figure 16 (b). We note that the condition for the dynamic aperture to extend beyond fifteen times the injected beam size is not quite satisfied.

4.3.3 Systematic Field Errors in the Sextupoles

The significant parameter for the dynamics is the sextupole gradient, i.e. the second derivative of the field. We assume that only components n = 8, 14, 20… are allowed by symmetry, and consider the effect of the lowest allowed component. We note that the total variation in the sextupole gradient at radius r_0 is given by:

$$\frac{\Delta g_s}{g_s} = \frac{1}{k_2}\sum_n \frac{k_n r_0^{n-2}}{(n-2)!}$$

With a single component $k_8 = 1.5\times10^{11}$m^{-7} k_2, the variation in the sextupole gradient is 0.35% at the internal beam pipe radius of 0.016 m, and at the pole tip (0.020 m), the variation is 1.3%.

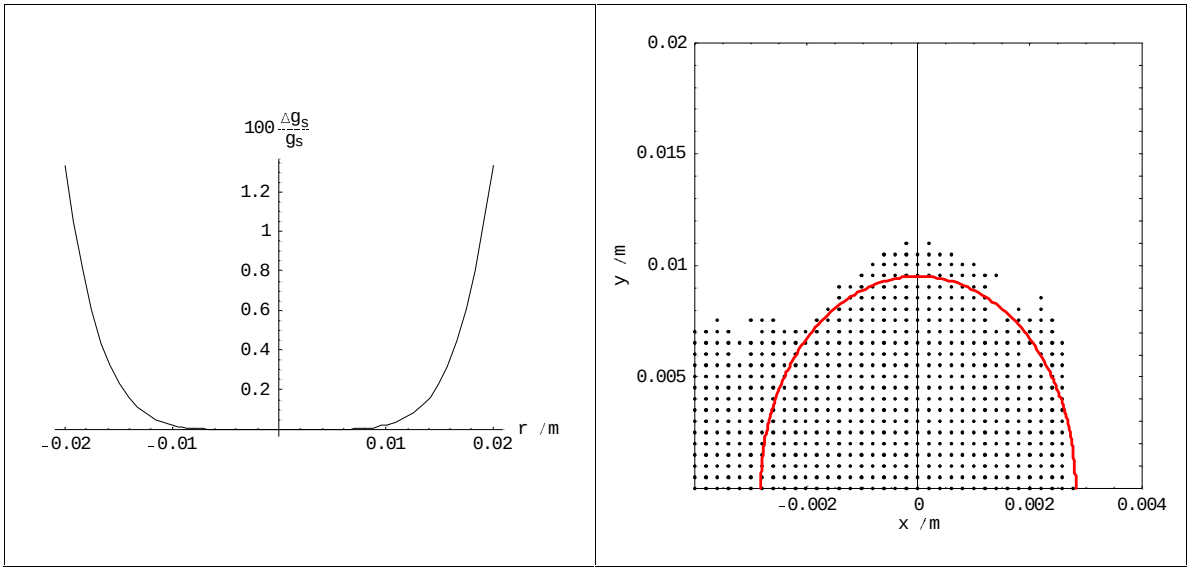

(a) (b)

Figure 17

(a) Variation in sextupole gradient arising from a single multipole component k_8 = 1.5×10^{11} m^{-7} k_2 and (b) resulting dynamic aperture

The corresponding dynamic aperture is shown in Figure 17 (b). Again, we note that the requirement for the dynamic aperture to be fifteen times the injected beam size is barely met.

4.3.4 Effects of Combined Systematic Errors

In practice, one often finds the dynamic aperture dividing into a "soft" outer halo and a "hard" inner core. In the soft region, the dynamics are strongly nonlinear, but stable; however, small changes to the lattice, as caused for example by field errors, will often lead to orbits in the soft region becoming unstable. In the hard region, by contrast, the nonlinearities may be treated as small perturbations to the dynamics, and the stability of orbits in this region is often robust against changes to the lattice. One might hope, therefore, that combining the systematic errors on the dipoles, quadrupoles and sextupoles, will not lead to significantly greater loss than is seen with each set of errors separately. This hope is somewhat justified in Figure 18, which shows the combined effects of the systematic errors applied above to the dipoles, quadrupoles and sextupoles separately. The corresponding variation in the field for each magnet type is given in Table 3.

Table 3

Variation in field quality from systematic field errors, leading to dynamic aperture shown in Figure 18

Magnet type	Variable	Variation at r_0 = 0.016 m	Variation at r_0 = 0.020 m
Dipole	$\frac{\Delta B}{B}$	0.06%	0.1%
Quadrupole	$\frac{\Delta g}{g}$	0.04%	0.1%
Sextupole	$\frac{\Delta g_s}{g_s}$	0.35%	1.3%

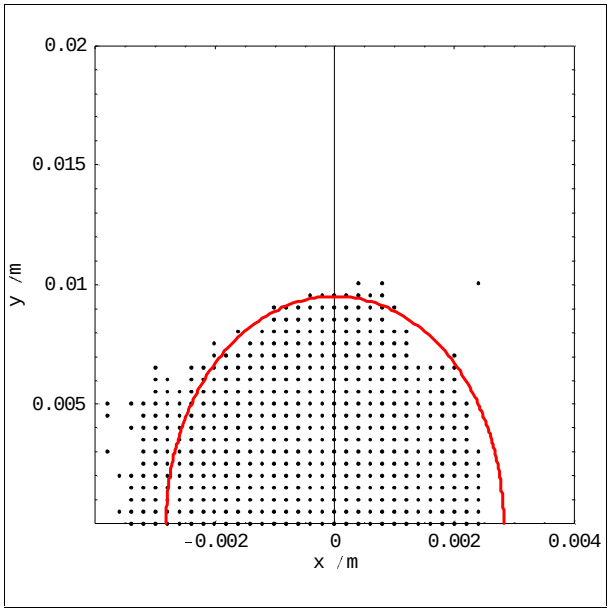

Figure 18

Dynamic aperture with combined systematic errors in dipoles, quadrupoles and sextupoles.

5 Systems in the Injection/Extraction Straight

5.1 Circumference Correction Chicane

A chicane provides the possibility of making small corrections to the circumference without the need to adjust the RF frequency. The small momentum compaction in the main damping rings makes them sensitive to changes in circumference arising from, for example, thermal effects, or running with the wiggler turned off (expected circumference change ~1.7 mm). We have retained an earlier design for a chicane, based on four rectangular dipole magnets, which allows a correction of the circumference over a range ±2 mm. Compensation for the focusing effects of the chicane magnets must be made by adjusting the quadrupoles in the adjacent matching section and the injection/extraction straight; initial studies suggest this will not cause any problems. The length of the chicane is 3.8 m, which allows it to fit in a 4.6 m drift section of the injection/extraction straight, with a drift of 0.3 m between the faces of the outside dipoles and the nearest quadrupoles.

5.2 RF Cavities

The relatively low RF voltage (1.07 MV) required to achieve a momentum acceptance of ±1.5% means that it might be possible to use just two cavities in each main damping ring. However, the present intention to use three cavities will allow some overhead for increased voltage, should improved acceptance prove necessary. Each cavity will require approximately 1 metre of free space[6]; the drift length between quadrupoles in the injection/extraction straight is 4.397 m, so three cavities should be accommodated comfortably in one such drift length. To avoid transients arising from variations in beam loading during injection/extraction, the cavities must be placed before the extraction kicker. In this case, no transients are induced as long as injection occurs simultaneously with extraction.

5.3 Extraction/Injection

The extraction/injection components have been positioned according to space constraints and the required phase advances. The components are represented in the deck by zero-bend dipoles, of lengths as specified in the ZDR[7]. Each system consists of a kicker (1.2 m length with a kick angle of 2.5 mrad) and a pair of septa (0.83 m, 25 mrad thin blade and 1.0 m, 90 mrad thick blade). The phase advance between the kicker and the septa is $0.25 \times 2\pi$ horizontally, so that the horizontal momentum change from the kicker is converted into a maximum transverse displacement at the first septum. The rise/fall time of the kickers is assumed to be 65 ns, which is slightly less than the gap between bunch trains, though it is to be expected that the following stored train will see some of the falling edge of each kicker. For this reason, the kickers are positioned with a phase advance of a half integer horizontally, so that the momentum kick from the falling edge of the first kicker can be compensated by a controlled momentum kick from the second kicker.

6 Effects of Magnet Misalignments

6.1 Closed Orbit Distortion

The vertical closed orbit is affected mainly by vertical quadrupole misalignments, and the horizontal closed orbit by horizontal quadrupole misalignments. The closed orbit response in each plane is shown in Figure 19, for 1000 seeds of quadrupole misalignments with rms between 0 and 10 μm. A gaussian distribution is applied in each case, with a cut-off at three times the standard deviation. There is significant scatter on the data, but an amplification factor may be found from the gradient of a least-squares fit. In the horizontal plane, the amplification factor is approximately 23.6, while in the vertical plane, it is significantly larger, with a value of 43.6. The large vertical amplification is of some concern, since vertical orbit distortion gives a significant vertical emittance, and the performance of the damping ring is critically dependent on achieving a low emittance coupling.

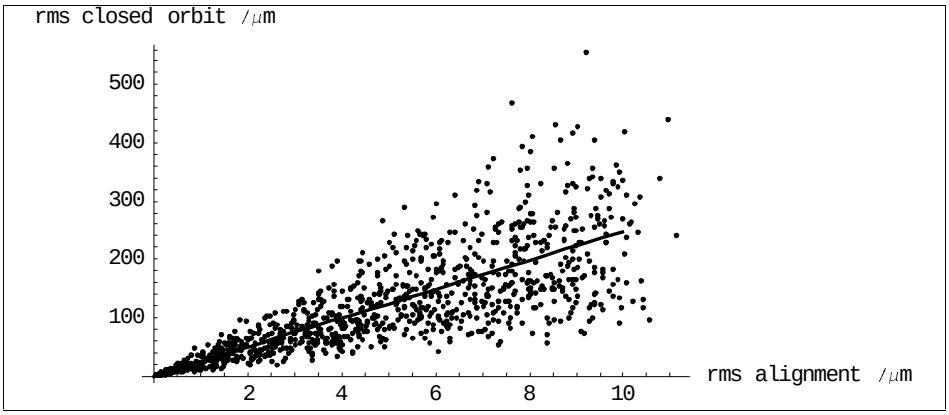

Figure 19 (a)

Horizontal closed orbit distortion for 1000 seeds of quadrupole horizontal misalignment. The line shows a fit with gradient 24.7.

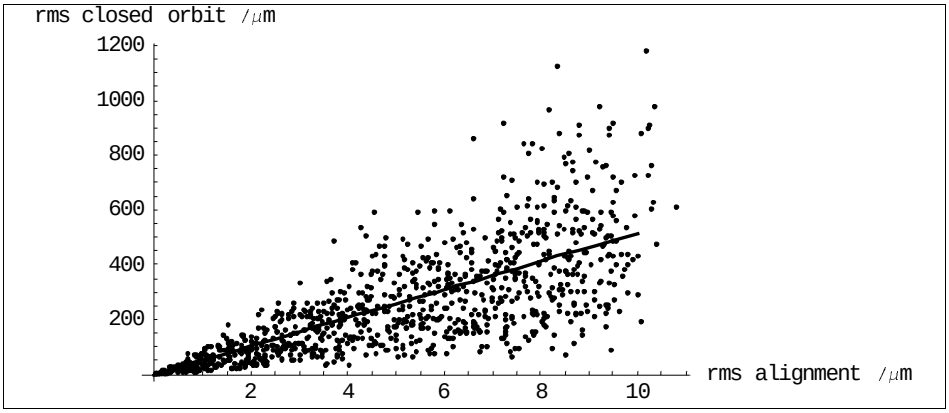

Figure 19 (b)

Vertical closed orbit distortion for 1000 seeds of quadrupole vertical misalignment. The line shows a fit with gradient 51.5.

6.2 Closed Orbit and Emittance Coupling

Vertical closed orbit distortion leads to a growth in vertical emittance because of three effects:

- vertical dispersion resulting directly from vertical steering;
- betatron coupling from vertical orbit offset in the sextupoles;
- dispersion coupling from vertical orbit offset in the sextupoles.

Assuming that the sextupole coupling is the dominant effect, a simple treatment of the coupling suggests a quadratic relationship between the closed orbit distortion and the vertical emittance, with the coupling constant given by:

$$g \approx 2\frac{N^2}{\Delta^2}\overline{\left(k_2 l\sqrt{\beta_x\beta_y}\right)^2}\,\overline{\delta y^2}$$

where N is the number of sextupoles, $k_2 l$ is the integrated sextupole gradient, and Δ is the distance to a nearby coupling resonance. The sextupole strengths and corresponding beta functions are given in Table 4. The tunes of a single cell are Q_x = 0.6253, and Q_y = 0.2685, which give Δ = 0.357 for the difference resonance, and Δ = 0.106 for the sum resonance; we expect a value for g between 10^{-4} and 10^{-3} %/μm^{-2}.

Table 4

Sextupole strengths and beta functions in an arc cell.

Sextupole	$k_2 l$	β_x	β_y
SX	23.82	4.0	2.2
SY	-17.76	1.1	9.0

The correlation between coupling and rms closed orbit is clearly shown in Figure 20, where we plot the vertical emittance as a function of the closed orbit distortion resulting from a quadrupole misalignment between 0 and 1 μm. No misalignments are applied to the dipoles or sextupoles. The quadratic coefficient is 5.71×10^{-4} %/μm^{-2}, in good agreement with our semi-analytical model.

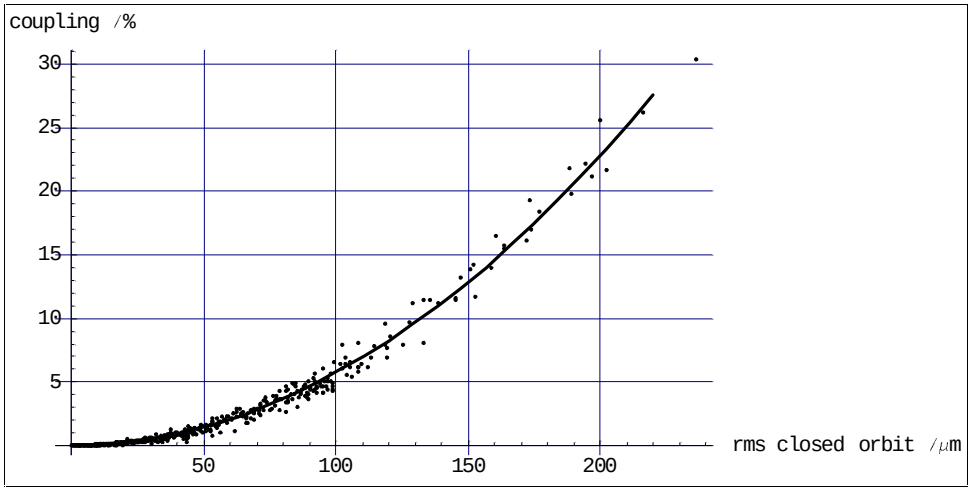

Figure 20

Emittance coupling as a function of vertical closed orbit distortion. The line shows a quadratic fit with coefficient 5.71×10^{-4} %/μm^{-2}.

The emittance coupling κ that may be expected from an rms orbit distortion σ_y may be estimated from:

$$\kappa = \alpha_2 \times (\alpha_1 \sigma_y)^2$$

where $\alpha_1 = 51.5$ is the linear amplification factor, and $\alpha_2 = 5.71\times10^{-4}$ %/μm^{-2} is the coefficient relating the rms closed orbit to the coupling. This formula suggests that to achieve a coupling of 0.5%, the positioning of the quadrupoles would have to be better than 0.6 μm rms. We note, however, that the scatter in Figure 19 indicates that relatively low orbit distortion may be achieved even with rms misalignments of several microns; the significant quantity is the rms closed orbit distortion.

6.3 Orbit Correction Scheme

To investigate the possibility of achieving low emittance coupling in the presence of quadrupole and sextupole misalignments, we construct a simulation based on the simple model shown in Figure 21. Each quadrupole is placed on an individual girder, with a magnet mover allowing vertical movement of the quadrupole in predefined steps. We assume that the dipoles are correctly aligned, and that the sextupoles have some vertical displacement. Each quadrupole has a BPM fixed to it. Vertical displacement of a girder results in misalignment of the mover, magnet and BPM (see Figure 21). Orbit correction follows a simple, standard algorithm, where a response matrix is first constructed relating changes in the BPM readings to changes in the mover positions. The response matrix is inverted by singular value decomposition, and the SVD inverse applied to the BPM readings to determine the displacements that should be applied to the magnet movers to effect the orbit correction. In principle, only one correction step is required, but in practice, the response matrix is a linear approximation valid for small orbit distortions; several iterations are then needed to achieve full correction.

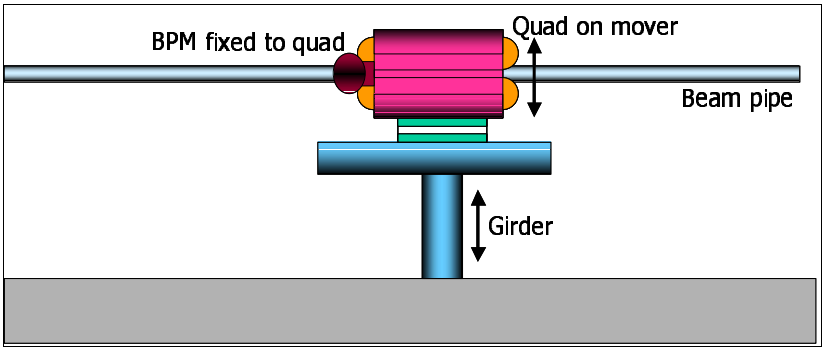

Figure 21

Quadrupole and BPM support structure for orbit correction model.

The residual orbit distortion after correction depends on several factors:

- the precision of the response matrix;
- the number of singular values set to zero in the singular value decomposition;
- the resolution of the BPMs;
- the precision with which the BPM-quadrupole offsets are known;
- the resolution of the magnet movers.

Beam-based alignment techniques applied at the ALS[8] have shown that BPM-quadrupole offsets may be determined with a precision of approximately 5 μm; the reported BPM resolution was also 5 μm. It is reasonable to assume that the BPMs used in the NLC damping rings will achieve a resolution somewhat better than this, and that the BPM-quadrupole offsets will similarly be determined with a better precision.

6.4 Results of Orbit Correction Simulations

The results of our simulation, with 1 μm step size on the magnet movers, and BPM to quadrupole offsets equal to the BPM resolution, are shown in Figure 22. For BPM resolution below about 10 μm, the dependence of vertical emittance on the resolution is fairly weak. The residual coupling at ideal resolution is consistent with a quadrupole alignment error of approximately 0.3 μm rms; this may be expected from a mover step size of 1 μm.

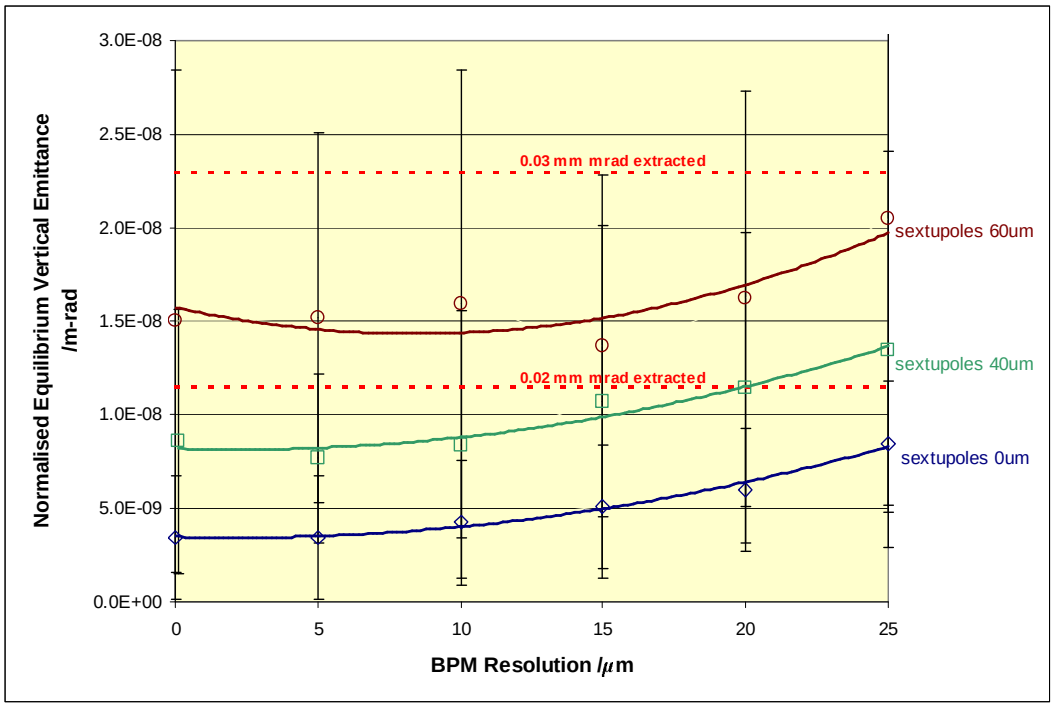

Figure 22

Normalised equilibrium vertical emittance as a function of BPM resolution, for various sextupole rms alignments. A step size of 1 μm has been used for the quadrupole movers, and the BPM to quadrupole alignment is assumed equal to the BPM resolution. The limits to achieve 0.03 mm mrad and 0.02 mm mrad extracted vertical emittances are shown.

We can also study the effect of reducing the mover step size; the results are shown in Figure 23. We have assumed 1 μm resolution on the BPMs, and 40 μm rms alignment on the sextupoles (with a cut off at 120 μm). It appears that there may be some benefit from reducing the step size to 0.8 μm or better. Our results suggest that an extracted emittance of 0.02 mm mrad may be achieved with a BPM resolution of 1 μm, a sextupole alignment of 40 μm rms, and quadrupole mover step size of 0.8 μm.

We note that there is significant scatter in the vertical emittance achieved after orbit correction for any given set of conditions; this is reflected in the large vertical error bars on the points in Figure 22 and Figure 23. However, we can be confident that the required vertical emittance can be achieved with the tolerances we specified above; the results of 200 seeds of alignment errors are shown in Figure 24. We assumed 1 μm BPM resolution, mover step size of 0.8 μm and 40 μm rms vertical sextupole misalignments. 90% of cases allowed a coupling correction to bring the normalized equilibrium vertical emittance below 0.0115 mm mrad, and hence the normalized extracted vertical emittance below 0.02 mm mrad.

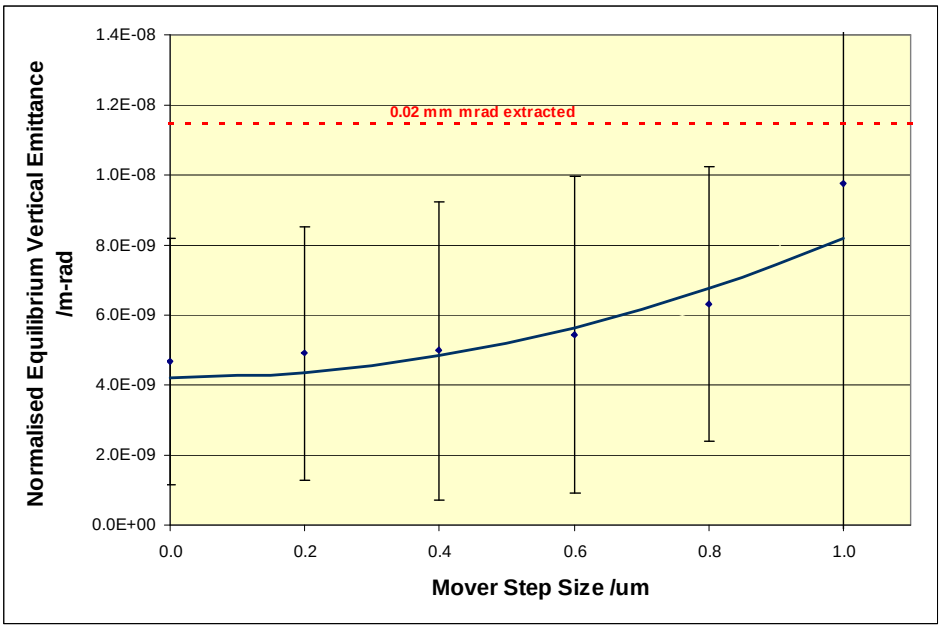

Figure 23

Normalised equilibrium vertical emittance as a function of mover step size. A BPM resolution of 1 μm is assumed, and sextupole alignment error of 40 μm rms. The limit to achieve 0.02 mm mrad extracted vertical emittance is shown.

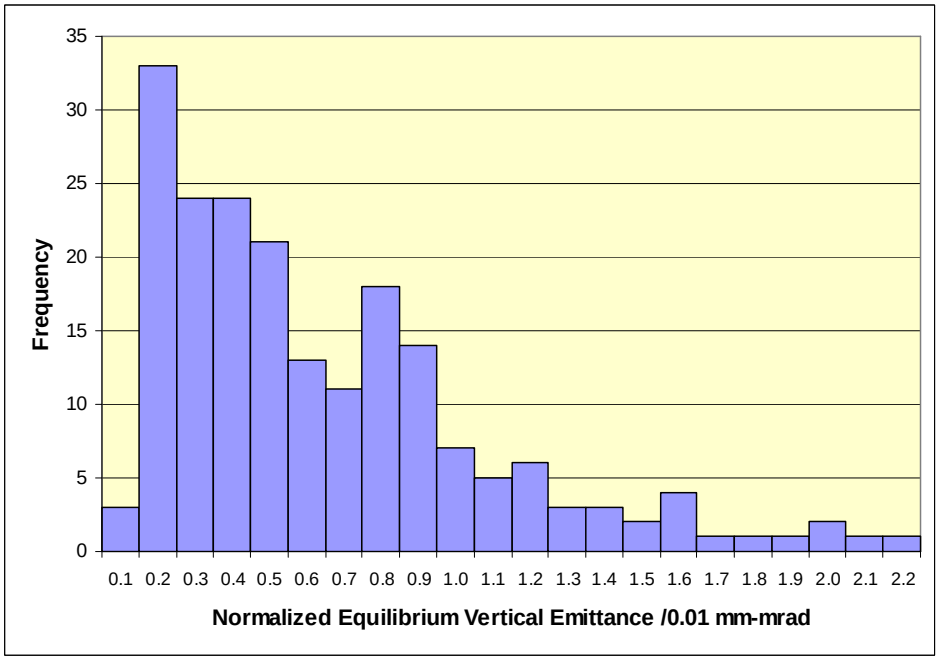

Figure 24

Equlibirium vertical emittance for 200 seeds of alignment errors; BPM resolution 1 μm, sextupole misalignment 40 μm and mover step size 0.8 μm. 90% of cases give an normalized equilibrium vertical emittance below 1.15×10^{-8} mm mrad, the limit for achieving an extracted emittance of 0.02 mm mrad.

7 Summary of Magnet Parameters

A summary of the parameters for the magnets used in the present lattice design is shown in Table 5.

Table 5

Magnet parameters in present main damping ring lattice design.

Type	Name	Location	Length	Pole-tip Radius /m	Normalised Field	Pole-tip Field /T	Count
Gradient Sector Dipole	BB	Arc	0.96		$k_0 = 0.1828$ m^{-1} $k_1 = -1.000$ m^{-2}	$B_0 = 1.2$	34
Gradient Sector Dipole	HBBMF	Arc to injection matching	0.48		$k_0 = 0.1828$ m^{-1} $k_1 = -0.9349$ m^{-2}	$B_0 = 1.2$	2
Gradient Sector Dipole	HBBMW	Arc to wiggler matching	0.48		$k_0 = 0.1828$ m^{-1} $k_1 = -1.3027$ m^{-2}	$B_0 = 1.2$	2
Quadrupole	QAF	Arc	0.25	0.02	$k_1 = 5.6249$ m^{-2}	0.7430	68
Quadrupole	QAD	Arc	0.25	0.02	$k_1 = -3.7802$ m^{-2}	-0.4993	32
Quadrupole	Q2MAF	Arc to injection matching	0.15	0.02	$k_1 = -5.3858$ m^{-2}	-0.7114	2
Quadrupole	Q1MAF	Arc to injection matching	0.25	0.02	$k_1 = 5.9844$ m^{-2}	0.7905	2
Quadrupole	Q1MF	Arc to injection matching	0.25	0.02	$k_1 = -1.8265$ m^{-2}	-0.2413	2
Quadrupole	Q2MF	Arc to injection matching	0.25	0.02	$k_1 = 2.8911$ m^{-2}	0.3819	1
Quadrupole	Q2MCH	Arc to injection matching (chicane)	0.25	0.02	$k_1 = 2.9094$ m^{-2}	0.3843	1
Quadrupole	Q1CH	Injection straight (chicane)	0.15	0.02	$k_1 = -1.6068$ m^{-2}	-0.2122	1
Quadrupole	Q1F2	Injection straight	0.15	0.02	$k_1 = -1.6526$ m^{-2}	-0.2183	3
Quadrupole	Q2F2	Injection straight	0.15	0.02	$k_1 = 2.4912$ m^{-2}	0.3291	3
Quadrupole	Q1F3	Injection straight	0.15	0.03	$k_1 = -1.6526$ m^{-2}	-0.3274	2
Quadrupole	Q2F3	Injection straight	0.15	0.03	$k_1 = 2.4912$ m^{-2}	0.4937	2
Quadrupole	Q2MAW	Arc to wiggler matching	0.15	0.02	$k_1 = -5.4754$ m^{-2}	-0.7233	2
Quadrupole	Q1MAW	Arc to wiggler matching	0.25	0.02	$k_1 = 6.0252$ m^{-2}	0.7959	2
Quadrupole	Q1MW	Arc to wiggler matching	0.25	0.02	$k_1 = -2.7733$ m^{-2}	-0.3663	2
Quadrupole	Q2MW	Arc to wiggler matching	0.25	0.02	$k_1 = 4.3788$ m^{-2}	0.5784	2
Quadrupole	Q1W	Wiggler straight	0.15	0.02	$k_1 = 2.0573$ m^{-2}	0.2718	4
Quadrupole	Q2W	Wiggler straight	0.15	0.02	$k_1 = 1.0543$ m^{-2}	0.1393	5
Sextupole	SX	Arc	0.06	0.02	$k_2 = 397.1$ m^{-3}	0.5245	68
Sextupole	SY	Arc	0.06	0.02	$k_2 = -295.7$ m^{-3}	-0.3906	68

8 Summary of Results

The lattice we have described in this note meets the main design criteria:

- sufficiently fast damping and low natural emittance to meet requirements on extracted emittance;
- dynamic aperture in excess of fifteen times the injected beam size (for zero-momentum deviation), which should allow good injection efficiency;
- circumference correction chicane capable of correcting over a range ±2 mm;
- sufficient room for RF cavities;
- injection/extraction kickers and septa positioned according to phase advance constraints.

In addition, the tolerances on magnetic field quality and alignment (with orbit control) look achievable. We have found that with the systematic field variations given in Table 3, the dynamic aperture remains in excess of fifteen times the injected beam size. We have not yet included the effects of random errors, which are expected to be significant.

Table 3

Variation in field quality from systematic field errors, leading to dynamic aperture shown in Figure 18

Magnet type	Variable	Variation at r_0 = 0.016 m	Variation at r_0 = 0.020 m
Dipole	$\frac{\Delta B}{B}$	0.06%	0.1%
Quadrupole	$\frac{\Delta g}{g}$	0.04%	0.1%
Sextupole	$\frac{\Delta g_s}{g_s}$	0.35%	1.3%

The coupling required to achieve an extracted emittance of 0.02 mm mrad is below 0.5%. Our simulations of orbit control, based on a simple alignment model, suggest that this is achievable with BPM resolution of 1 μm, mover step size of 0.8 μm, and sextupole alignment of 40 μm. These tolerances could be loosened significantly by the use of a skew correction system, using skew quadrupole windings on the sextupoles. Investigations of such a system are planned.

The narrow momentum acceptance is a concern, with the dynamic aperture falling rapidly beyond momentum deviations of around 0.5%. The global higher order chromaticities are well corrected, with the tune variation small up to 1.5% momentum deviation. It seems likely that the momentum acceptance is being limited by a breakdown of the integer phase advance over the straight sections. It is not clear at present how this problem may be addressed. We note that the full width energy spread of the beam (after energy compression) injected into the main damping ring, is 0.5%.

The dynamics studies presented in this note have treated the wiggler as a linear element; studies of the effects of nonlinear fields in the wiggler, resulting primarily from finite pole widths, have been carried out and are reported in a separate note[4].

References

[1] P.Emma and T.O.Raubenheimer, "*A Systematic Approach to Damping Ring Design*", Phys.Rev.ST Accel.Beams 4:021001, 2001.

[2] P.Emma, Private Communication, April 1999.

[3] H. Nishimura, Private Communication, September 2000.

[4] A.Wolski, "*Symplectic Integrators for Nonlinear Wiggler Fields*", CBP Tech. Note 288, LCC-0062, April 2001.

[5] A.Wolski, "*Improved Dynamics in the 180 Hz NLC Damping Rings*", CBP Tech. Note 223, LCC-0055, February 2001.

[6] R.Rimmer et al, "*RF Cavity R&D at LBNL for the NLC Damping Rings*", LCC-0033, December 1999.

[7] The NLC Design Group, "*Zeroth-Order Design Report for the Next Linear Collider*", LBNL-PUB-5424, SLAC Report 474, UCRL-ID-124161, May 1996. pp.242-245.

[8] D.Robin, G.Portmann, L.Schachinger, "*Automated Beam Based Alignment of the ALS Quadrupoles*", NLC Note 18, August 1995.